ELSEVIER

Journal of Structural Geology 29 (2007) 1430–1444

JOURNAL OF STRUCTURAL GEOLOGY

www.elsevier.com/locate/jsg

# Objective fitting of ellipses in the centre-to-centre (Fry) method of strain analysis

John W.F. Waldron*, K.D. Wallace

*Department of Earth and Atmospheric Sciences, University of Alberta, Edmonton, Alberta, Canada T6G 2E3*

Received 1 March 2007; received in revised form 15 June 2007; accepted 15 June 2007
Available online 10 July 2007

**Abstract**

Centre-to-centre measurements are used in the Fry method of estimating fabric ellipses for strain analysis. Despite the usefulness of the method, estimation of the elliptical shape of the central vacancy field in a Fry plot is typically subjective. Two new methods can provide more objective estimates of the fabric ellipse by locating the locus of maximum point-density gradient. The point-count density method compares the number of points in a central elliptical area with the number in a surrounding annulus having the same area. By varying the dimensions of the ellipse it is possible to maximize the point-density contrast between the inner ellipse and the surrounding annulus, providing an estimate of the shape of the fabric ellipse. The continuous function method uses an exponential function to measure the fit of points in the Fry plot to a trial ellipse. By varying the dimensions of the trial ellipse, it is possible to maximize the value of this function, providing a second estimate of the shape of the fabric ellipse. Both methods use the image processing software ImageJ, although the search for the optimum ellipse in the continuous function method is more rapidly executed using the Solver program in Microsoft Excel.


*Keywords:* Fabric analysis; Strain ellipse; Centre-to-centre; Fry method

## 1. Introduction

Measurements of the distances and directions between object centres are widely used in the 'centre-to-centre' method of strain analysis to determine the two-dimensional finite strain in naturally deformed rocks. Results are typically presented graphically for interpretation in the form of Fry (1979) plots, in which the distances and directions between pairs of objects are represented by dots, placed at the same distance and direction relative to the origin of a graph. Suitable initial distributions of objects produce Fry plots with an elliptical vacancy field in the central part of the plot. If the original distribution of objects is isotropic, the shape of the vacancy field represents the shape of the finite strain ellipse.

However, the interpretation of Fry plots can be subjective. Different observers judge the shape of the vacancy field ellipse differently. Proposed methods for objectively fitting an ellipse (e.g. Erslev and Ge, 1990) rely on identifying those points in the plot that represent objects that were originally in contact. For some types of objects this is difficult or impossible. The starting point for this study was our desire to objectively fit an ellipse to an anticlustered array of dewatering pipes on a bedding surface (Fig. 1a) in the Windermere Supergroup in the Cariboo Mountains of the Canadian Cordillera. Because the objects are effectively points, with no measurable size or shape, the method of Erslev and Ge (1990) could not be applied. In this paper, we propose two new methods for defining a best-fit elliptical boundary for the central vacancy field, to provide more objective estimates of the shape and orientation of the fabric ellipse. These methods use a combination of image processing software (ImageJ) originally developed for medical imaging (Abramoff et al., 2004), and spreadsheet software (Microsoft Excel).

* Corresponding author.
*E-mail address:* john.waldron@ualberta.ca (J.W.F. Waldron).

0191-8141/$ - see front matter © 2007 Elsevier Ltd. All rights reserved.
doi:10.1016/j.jsg.2007.06.005

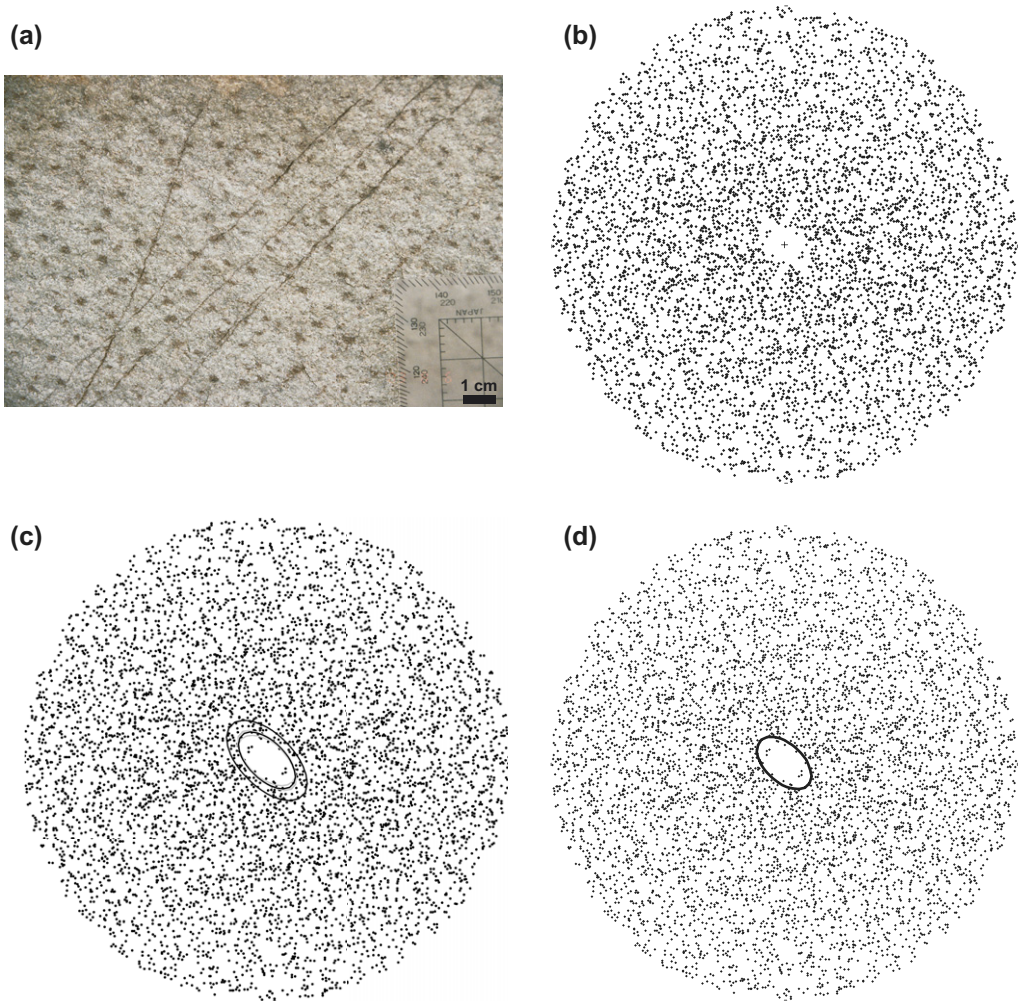


Fig. 1. (a) Bedding surface in turbidites of Kaza Group, Windermere Supergroup, at Castle Creek in the Cariboo Mountains of British Columbia, Canada. Dark spots are interpreted as dewatering pipes. (b) Uninterpreted Fry plot showing poorly defined central vacancy field; $n = 127$. (c) Fry plot with interpreted fabric ellipse prepared by point-count density method in FryJFit. (d) Fry plot with interpreted fabric ellipse prepared by continuous function method in FryXFit.

## 2. Previous work

Centre-to-centre methods of strain analysis (Ramsay, 1967) require the assumption of a statistically isotropic initial distribution of objects in which objects were anticlustered – i.e. they were unlikely to be closer than a certain minimum distance apart. The radial plotting method of Fry (1979) was developed into an elegant graphical technique by Hanna and Fry (1979), using a sheet of tracing film repeatedly placed with its centre over an object; the relative positions of all surrounding objects are plotted until a central vacancy field emerges. Fry plots are particularly effective in the estimation of bulk strain in rocks where the shapes of deformed objects are either invisible or provide a poor guide to bulk strain. For example, sedimentary structures, such as dewatering pipes (Fig. 1a) and sand volcanoes (Waldron and Jensen, 1985; Waldron, 1988), may display diffuse outlines but nonetheless show anticlustered distributions. Also, in rocks where pressure solution removed original grain-boundaries, valid estimates of the bulk strain can be obtained by the Fry method (e.g. Ramsay and Huber, 1983), although Dunne et al. (1990) and Onasch (1986) caution that the difficulties in identifying the location of original object centres may introduce bias.

The usefulness and accuracy of the Fry plot depend on the sharpness of the vacancy field, which, in turn, depends on the degree of anticlustering and the number of objects in the sample (Fry, 1979). The most difficult problem with the method is the subjectivity of visually fitting an ellipse, especially when the field is vaguely defined (Crespi, 1986; Longiaru and Bhattaharyya, 1985). A method for improving the definition of the vacancy field is suggested by Erslev (1988) who shows how each interparticle distance can be divided by the sum of the average radii of the two particles involved. The resulting normalized Fry (or NFry) plot may remove much of the blurring effect of poor sorting. However, this valuable technique cannot be applied to distributions of features such as dewatering structures, where the dimensions of the original objects cannot be determined.

Several authors have suggested methods for objectively estimating the shape of the fabric ellipse. Erslev and Ge (1990)

construct enhanced Fry (ENFry) plots for granular rocks by eliminating points representing grains not in contact. The determination of whether grains are in contact is made from elliptical approximations of grain shape. Points separated by more than a certain threshold distance (compared to the ellipse radii) are eliminated; ideally, the remaining points are clustered in a narrow girdle surrounding the vacancy field; Erslev and Ge (1990) use a least-squares algorithm to fit an ellipse through this girdle. In practice, the ENFry approach is difficult to apply to some strain markers. First, for features such as the dewatering structures shown in Fig. 1, there is no information on 'grain' shape to calculate nearest-neighbour relationships, and the method cannot be applied. Second, in granular materials in which pressure solution has occurred, adjacency relationships between grains may have been strongly modified during deformation. Finally, even where distorted grain outlines are clear, if grain shapes are highly irregular then the 'in-contact' relationships calculated in the ENFry method are significantly different from the true contact relationships, potentially resulting in a very diffuse girdle of points. In such cases, a subjective operator judgment is required to determine the threshold distance beyond which grains are not considered 'in-contact'. For poorly defined girdles, selection of this arbitrary parameter may bias the result.

Ailleres and Champenois (1994) applied image processing to join the images of dots so as to isolate the shape of the vacancy field. However, the isotropic transformation applied to enlarge the dots may modify the proportions of the vacancy field, especially at low point densities and large strain ratios. The experimental results obtained by Ailleres and Champenois (1994) slightly underestimate the true axial ratios. McNaught (1994) used a polar gridding of the Fry plot to 'bin' the points and then investigate their distribution between grid cells. Noting that the shape of grid cells can introduce a bias to the ellipse shape, McNaught progressively and iteratively unstrained the Fry plot until the points were isotropically distributed, yielding an unbiased, though computationally intensive, estimate of the strain ratio. The method does require a somewhat arbitrary choice of grid size for binning, which may be difficult where the density of points is low or the boundary of the vacancy field is poorly defined.

## 3. Criteria

It is helpful to consider the distribution of points in Fry plots in more detail. So, we distinguish between 'objects' in the original distribution, and 'points' in the resulting Fry plot.

### 3.1. Characteristics of random (Poisson) distributions

A distribution of objects generated by a spatially completely random (or Poisson) process shows no anticlustering (Fig. 2a) (Fry, 1979). Such a distribution cannot be used to measure strain. However, the properties of Poisson distributions are important to consider, as a basis for comparison with strained anticlustered distributions. If $n$ random objects are selected from a Poisson distribution, and all neighbouring objects (up to some limiting radius $f$) are used to prepare a Fry plot, no central vacancy field appears. In fact the Fry plot is also a Poisson distribution, and has a statistically uniform density of points out to radius $f$ (Fig. 2b, c). If the parent distribution has some density (objects/area) $\rho_0$, then the expected density of points ($\rho$) expressed as points per unit area in the Fry plot is given by (Appendix 1):

$$\rho = N/\pi f^2 = n\rho_0 \tag{1}$$

where $N$ is the number of points and $f$ is the radius of the plot. The density of points is constant, regardless of the distance ($r$) and direction ($\theta$) from the centre (Fig. 3a). If, on the other hand, density is expressed as points per unit radius, then *radial*

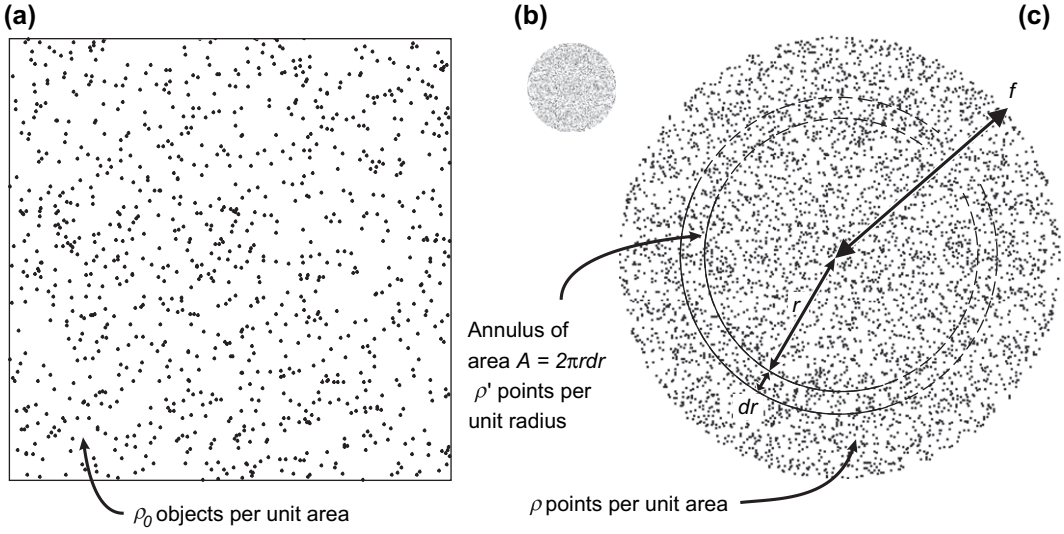


Fig. 2. (a) Random (Poisson) distribution of 1000 points distributed over a square of side 50 mm. (b) Fry plot generated from points in (a) with limiting radius $f = 5$ mm. (c) Enlarged version of (b), showing terms used in calculations of point density.

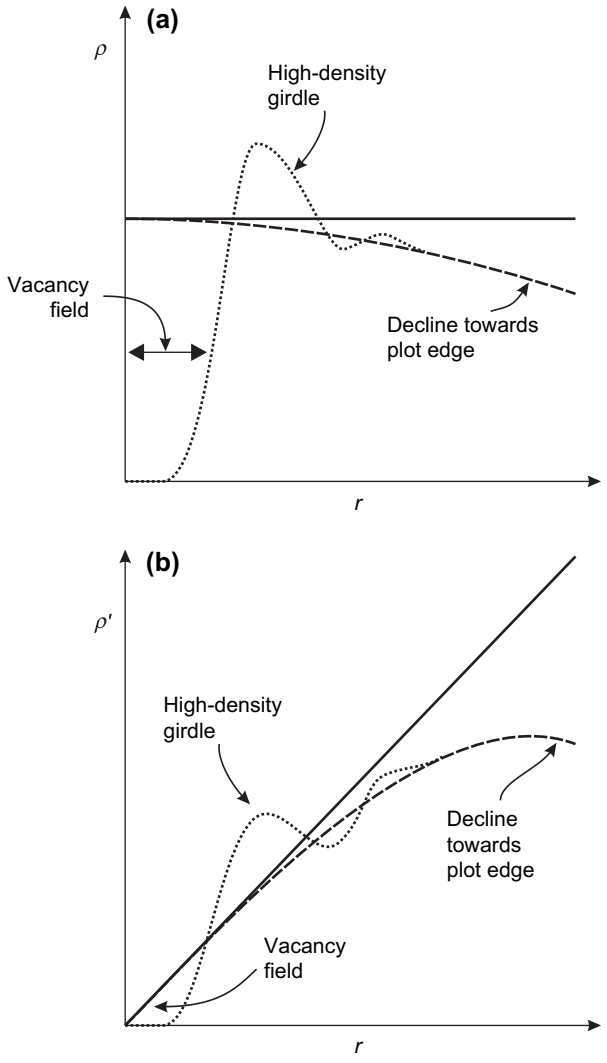


Fig. 3. (a) Schematic graph of density (points per unit area) with respect to radius in a Fry plot. Solid line represents random sampling of points from an infinite random distribution. Dashed line shows fall in density due to reduction of number of neighbours at the edge of the sampled area. Dotted line shows typical density variation in a plot prepared from an unstrained anticlustered distribution of objects. (b) Schematic graph of density measured as points per unit radius, plotted with respect to radius. Symbols as in (a).

*density* ($\rho'$) increases steadily with radius (Fig. 3b) according to:

$$\rho' = 2rN/f^2 = 2\pi r\rho \tag{2}$$

### 3.2. Density gradients in Fry plots of deformed rocks

In Fry plots from deformed rocks, the central vacancy field and any surrounding high-density girdles are distorted into elliptical shapes having the same aspect ratio as the strain ellipse. Points are rotated towards the extension axis but are also moved radially, with the result that, for nondilational strain, point densities ($\rho$) are unmodified. The most characteristic and well-defined elliptical feature of most Fry plots is the density gradient at the edge of the elliptical central vacancy field (Fig. 3). Ideally, this gradient represents the deformed shape of the 'clear region' around each anticlustered object. We seek an objective estimate of the fabric ellipse by fitting an ellipse to this locus of maximum gradient. We propose two methods of fitting such an ellipse. Each is based on constructing a trial ellipse, and then using a function of the point distribution to determine how well the trial ellipse coincides with the density gradient. In principle, we could also fit another ellipse to the outer edge of the first high-density girdle, and even subsequent girdles. We did not consider these outer gradients because they are commonly very diffuse and their positions relative to the inner gradient are dependent on the degree of anticlustering.

#### 3.2.1. Point-count density method

For the first method, two concentric, similarly oriented ellipses are constructed (Fig. 4a), so as to define a central trial ellipse (to fit to the vacancy field), and a surrounding, geometrically similar elliptical annulus (to fit the first high-density girdle, if present). The measure of goodness of fit that is used is the difference or contrast in the density of points between the inner ellipse and outer annulus.

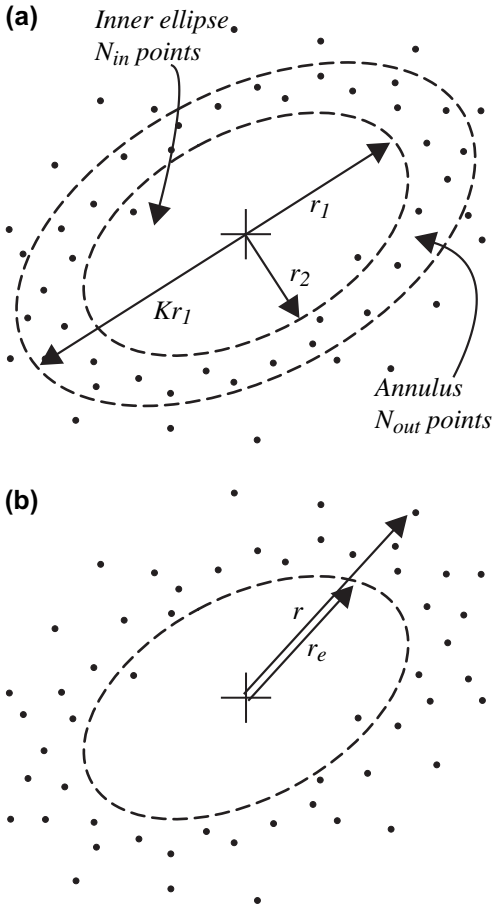


Fig. 4. (a) Diagram showing quantities used in the point-count density method. (b) Diagram showing quantities used in the continuous function method.

If $N_{out}$ and $N_{in}$ are the number of points in the annulus and the inner ellipse, respectively, then the density contrast ($C$) is given (Appendix 2) by:

$$C = \frac{f^2}{Nr_1r_2}\left(\frac{N_{out}}{(K^2-1)} - N_{in}\right) \quad (3)$$

where $r_1$ and $r_2$ are the major and minor radii of the inner ellipse, and $K$ is the ratio of the radii of the outer ellipse to those of the inner ellipse (Fig. 4a).

When a good fit is obtained, the inner ellipse matches the vacancy field and contains a low density of points, whereas the annulus matches the zone immediately outside the vacancy field, containing the highest point density. Systematic trials are used to find the ellipse that maximizes the value of $C$.

The choice of $K$ is somewhat arbitrary. Our initial trials used a $K$ value of $\sqrt{2}$. This value was chosen because: (i) for many Fry plots, it approximates the position of the density minimum separating the first girdle (at $r = D$) and the second high-density girdle (at $r = \sqrt{3}D$); and (ii) the areas of the inner ellipse and annulus are equal, simplifying the calculation. Subsequent trials using experimentally deformed images of objects with different $K$ values failed to improve on the results, demonstrating the general efficacy of the choice of $K = \sqrt{2}$.

As the radius ($r$), aspect ratio ($R$), and orientation ($\varphi$) of the trial ellipse vary, points drop in and out of the ellipse and the annulus; the value of $C$ therefore varies discontinuously. Accordingly, we anticipate a region of ($r$, $R$, and $\varphi$) space over which the value of $C$ will be a maximum, rather than a single point. The size of this region will depend on the number of points sampled in the Fry plot. Larger samples will produce a smaller, more tightly defined maximum. Because of the discontinuous variability of $C$ over the solution space, we needed to use the macro language in the image analysis program ImageJ (Abramoff et al., 2004) to write a program (FryJFit) to exhaustively search the solution space to maximize $C$ (see Section 4.3).

### 3.2.2. Continuous function method

Our second method involves a continuously varying measure of goodness of fit, rather than a discrete point-counting approach. In contrast to the least-squares method used by Erslev and Ge (1990), which is ideal for fitting a curve through a line of high-density points, we require a function that measures the extent to which points are concentrated *on one side* of a trial elliptical curve. We measure the deviation of each point ($x$) from the ellipse as a fraction of the radius ($r_e$) of the trial ellipse.

$$x = (r - r_e)/r_e = r/r_e - 1 \quad (4)$$

where $r$ is the distance of a point from the centre of the Fry plot, and $r_e$ is the radius of the trial ellipse in the same direction (Fig. 4b). Points inside the ellipse have negative $x$; points outside have positive $x$.

After experiments with a number of functions, a measure of deviation, for a single point, having the following general form was adopted:

$$y = xe^{-(kx)^2} \quad (5)$$

where $k$ is a constant and $x$ is defined as above. The measure $y$ has large positive values for small positive $x$, falls to near zero at larger $x$, has large negative values for small negative $x$, and rises to near zero at larger negative $x$ (Fig. 5). The quantity $y$ therefore represents a good measure of the degree to which a single point is consistent with a given trial ellipse.

We wish to sum the values of $y$ across all points in the Fry plot, so as to obtain an overall measure of ellipse fit. However, in summing the values of $y$, we have to consider that, even in a random (Poisson) plot, the linear density of points with respect to $r$ rises linearly with radius (Fig. 3b). Hence, outer parts of the plot will have a larger effect on the sum of the $y$ values than implied by the curve shown in Fig. 5. Accordingly, we define a corrected measure ($z$) in which the effect of points is reduced in proportion to their distance from the centre.

$$z = y/r = \frac{x}{r}e^{-(kx)^2} \quad (6)$$

To measure the goodness of fit for a given trial ellipse, we sum the values of $z$ over all $N$ points to obtain a measure of overall density contrast across the elliptical boundary.

$$Z = \sum_{i=1}^{N} z_i \quad (7)$$

The choice of $k$ is somewhat arbitrary; $k$ is inversely analogous to the radius ratio $K$ in the point-counting method; smaller values of $k$ are analogous to larger values of $K$,

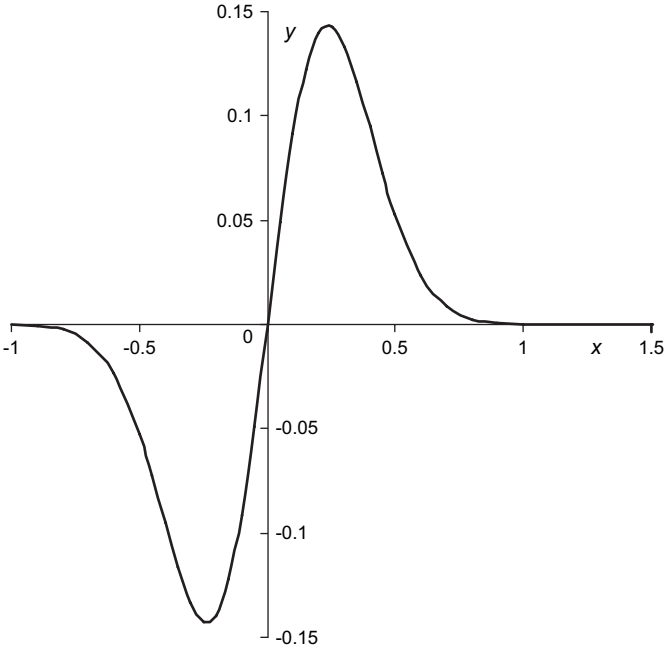


Fig. 5. Plot of the function $y = x\exp(-(kx)^2)$ used as a measure of the goodness of fit of a single point to a trial ellipse.

because they spread out the area over which $z$ has large values. Too small a value of $k$ will cause $Z$ to be sensitive to the distribution of points in the outer part of the Fry plot. On the other hand, if $k$ is set too large, only a few points close to the trial ellipse will have an effect on the value of $Z$, and a spurious ellipse may be fitted to a very small number of points. In principle, the ideal value of $k$ is dependent on the degree of anticlustering of the objects in the sample; highly anticlustered points should be fitted with large $k$ whereas poorly anticlustered samples would be expected to give best results with smaller $k$. In practice, our experiments with simulated distributions of points (see Table 1) have shown that an empirically determined $k = 3$ is generally effective.

To compare $Z$ and $k$ values between Fry plots with different values of radius ($f$) and number of points ($N$), we need to modify the calculation to consider the dependency of $Z$ on these quantities. As $Z$ is proportional to $N/f^2k^2$, we define a normalized test value (Appendix 3):

$$Z' = \frac{k^2 f^2}{N} \sum_{i=1}^{N} z_i \tag{8}$$

Because $Z'$ varies continuously, it is possible to search using an optimization routine in a spreadsheet program such as Microsoft Excel.

In experiments using object populations that differed only in spacing, but were otherwise identical, the optimum value of $Z'$ was found to scale linearly with object size. Accordingly, as shown in Appendix 4, it is appropriate, when comparing $Z$ values from plots with different grain size, to further scale $Z'$ using the major and minor axes of the optimum ellipse. We define the quantity $Z^*$ as:

Table 1
Effect of varying the concentration parameter $k$ on solutions obtained by the continuous function method

| Sample | True strain | | $k$ Parameter | | Estimated strain | |
|---|---|---|---|---|---|---|
| | Strain ratio | Orientation | | | Strain ratio | Orientation |
| 1 | 2.5 | 167 | Floating | 3.842 | 2.50 | 166.7 |
| | 2.5 | 167 | Fixed | 1.000 | 2.21 | 168.3 |
| | 2.5 | 167 | Fixed | 1.414 | 2.50 | 166.3 |
| | 2.5 | 167 | Fixed | 2.000 | 2.49 | 166.3 |
| | 2.5 | 167 | Fixed | 3.000 | 2.49 | 166.5 |
| | 2.5 | 167 | Fixed | 4.000 | 2.50 | 166.7 |
| | 2.5 | 167 | Fixed | 6.000 | 2.54 | 167.0 |
| | 2.5 | 167 | Fixed | 8.000 | 2.46 | 169.8 |
| 2 | 1.3 | 132 | Floating | 2.674 | 1.25 | 126.9 |
| | 1.3 | 132 | Fixed | 1.000 | 1.08 | 35.1 |
| | 1.3 | 132 | Fixed | 1.414 | 1.23 | 131.4 |
| | 1.3 | 132 | Fixed | 2.000 | 1.24 | 128.2 |
| | 1.3 | 132 | Fixed | 3.000 | 1.25 | 126.5 |
| | 1.3 | 132 | Fixed | 4.000 | 1.27 | 125.5 |
| | 1.3 | 132 | Fixed | 6.000 | 1.37 | 151.5 |
| | 1.3 | 132 | Fixed | 8.000 | 1.42 | 154.2 |

$$Z^* = \frac{Z'_{\mathrm{opt}}}{\sqrt{r_1 r_2}} \tag{9}$$

as a dimensionless measure of the fit represented by the optimum value of $Z'$, $Z'_{\mathrm{opt}}$.

## 4. Application

### 4.1. Image processing

The open-source, Java-based medical image processing program ImageJ (Abramoff et al., 2004) provides a convenient method of preparing Fry plots using images of objects in deformed rocks. ImageJ provides:

- Thresholding capability – pixels in an image can be automatically classified to distinguish objects from surrounding matrix.
- Object identification – objects in the thresholded image are automatically identified. A 'Results' listing is generated that includes the coordinates of object centres, their areas, and the major and minor axes and orientations of equivalent ellipses.
- Programmability – a simple macro language allows calculations and automated plotting based on the object parameters listed above.

To prepare a Fry plot using ImageJ, the first step is to create an image in which objects are clearly differentiated from surrounding matrix areas. Under ideal circumstances, this may be possible using the image processing capabilities of ImageJ. Our thin section and field photographs were sufficiently heterogeneous and complex that we found it necessary to manually identify the objects, by tracing them as black polygons on a separate layer in a graphics program (such as CorelDraw or Photoshop); the traced objects were exported as a greyscale TIFF image file.

The image file was then opened in ImageJ. ImageJ allows the operator to set a 'threshold' to separate objects from non-object background. This level was set in each case to eliminate anti-aliased grey pixels at the margins of objects, so as to ensure that all objects were separated from one another by at least one pixel of background. Next, ImageJ's 'Analyze Particles' command was used to identify all objects in the image and to produce a list of objects in a separate 'Results' window. For each object we specified the centroid $x$ and $y$ coordinates, the area, and the parameters of an equivalent ellipse: maximum and minimum diameters, and orientation. (The data listed for each particle are controlled from a separate 'Set Measurements…' dialog in ImageJ.) Note that the equivalent ellipses are calculated to have the same area and moments of inertia as the source polygons; this method of calculating equivalent ellipses is similar to that proposed by McNaught (1994), and differs slightly from the method originally used by Erslev and Ge (1990).

The data in the results window can be analysed by either Rf/phi or Fry method. For Rf/phi plotting, the results are best saved and imported into a spreadsheet. For Fry plotting, a program FryJ was prepared using the ImageJ macro language.

### 4.2. FryJ program

The macro FryJ, available as a supplementary file accompanying the digital version of this paper, reads data from the 'Results' window, and plots a Fry plot in a new window. An initial dialog (Fig. 6a) allows the user to set plotting parameters: the radius $f$ (in pixels) of the plot; the size of dots in the plot; whether the plot is to be normalized or enhanced; and whether the coordinates of points should be listed in a separate 'Log' window. A scaling factor gives the user control over the size of the resulting plot: for non-normalized plots the default value (100%) produces a Fry plot that is scaled exactly as the source image; for normalized plots the default normalizing radius is 100 pixels. For enhanced plots, the user has control over the Erslev and Ge (1990) threshold factor.

The program operates by looping through the $n$ objects listed in the 'Results' window. For each object, a second, nested loop passes through all the objects again, determining the distances and directions between every pair of object centroids. If the user has selected a normalized plot, the distances and directions are normalized according to the areas of the particles as proposed by Erslev (1988). If an enhanced plot is selected, then a calculation of the ellipse radii is used to determine whether the particles are within the threshold distance for contact (Erslev and Ge, 1990).

Before plotting, distances are compared with the plot radius ($f$) specified by the user; points beyond this radius are eliminated. Points outside the enhancement threshold (if any) are plotted in grey. Other points are plotted in black and their coordinates are listed (if this option has been selected) in the 'Log' window in ImageJ. At the end of plotting, the user may save the contents of the 'Log' window to a text file for further processing.

### 4.3. Ellipse fitting: systematic search

The log file saved from FryJ contains the coordinates of all points in the Fry plot. This file may contain up to $n^2 - n$ values. For even quite moderate data sets there may be several tens of thousands of points. A second macro program, FryJFit, also available as a supplementary file accompanying the digital version of this paper, searches systematically for maximum values of the statistics $C$ and $Z'$, defined above.

FryJFit reads coordinates of points from a text file. Initially the points are plotted in a re-created Fry plot. Next, the user specifies, in dialogs, the method (point-count density or continuous function) and the parameters for a search for an optimal solution (Fig. 6b, c). Parameters include maximum and minimum values of aspect ratio $R$, orientation $\varphi$, and minimum radius $r_{\min}$. In addition, the user can specify the increment between trial ellipses for all three parameters. The program then generates trial ellipses and calculates the value of $C$ or $Z'$ for each, optionally recording the results in the log window. The program also keeps a working list of the 10 best-fit solutions (maximum $C$ or $Z'$). At the conclusion of a run these are listed, and the corresponding ellipses are drawn on the plot (Fig. 6d).

Depending on the number of points in the plot, the range and 'fineness' of the search, and the speed and memory of the computer, runs can take minutes to tens of minutes to complete. For practical purposes, it is usually best to run a coarse search first, typically using 10° increments of $\varphi$, 0.1 increments of $R$ and 10 pixel increments of $r_{\min}$. The user then has the opportunity to refine the search, narrowing the search range from the first 'coarse' search to a restricted region of the solution space, and the search can be repeated with finer increments of $R$, $\varphi$, and $r_{\min}$, to refine the solution.

### 4.4. Ellipse fitting: spreadsheet solution

As an alternative to exhaustive searching, a method of finding the best-fit ellipse has been devised using Microsoft Excel's 'Solver' add-in. The spreadsheet FryXFit, available as a supplementary file accompanying the digital version of this paper, contains a data worksheet with space for up to 30,000 $x-y$ pairs representing the coordinates of points in a Fry plot. On a second worksheet labelled 'plot', these points are automatically plotted on a chart, reconstructing the Fry plot. Also on this sheet, the user can enter in the parameters $R$, $\varphi$, and $r_{\min}$, to define an ellipse that is automatically plotted on the chart (Fig. 7). The user also can vary the value of $k$, which is used in the calculation of $z$ for each point on the data sheet. These are summed to display $Z'$ on the plot sheet. The 'Solver' add-in for Excel allows a systematic search for the values of $R$, $\varphi$, and $r_{\min}$ which maximize $Z'$.

Solver solutions are faster than those obtained by systematic search. The solution algorithm used by Excel works well for strongly anticlustered data sets in which the edge of the vacancy field is well-defined. For weakly anticlustered data sets, the algorithm sometimes finds spurious local maxima in the value of $Z'$. This problem is greatly alleviated if the user supplies initial estimates for $R$, $\varphi$, and $r_{\min}$, which visually approximate the vacancy field; the solver algorithm typically has little difficulty in refining the estimate to obtain the true solution.

Attempts to use the Solver to maximize the point-counting density statistic $C$ failed because $C$ varies very discontinuously over the solution space. Several adjacent trial positions of the ellipse may contain the same number of points, resulting in constant $C$, whereas the solver is dependent on finding gradients of $C$ with respect to $R$, $\varphi$, and $r_{\min}$, in order to approach an optimal solution.

## 5. Testing

As a preliminary test of the proposed methods we have applied them to a number of examples with known strain, including simulated two-dimensional arrays of objects having

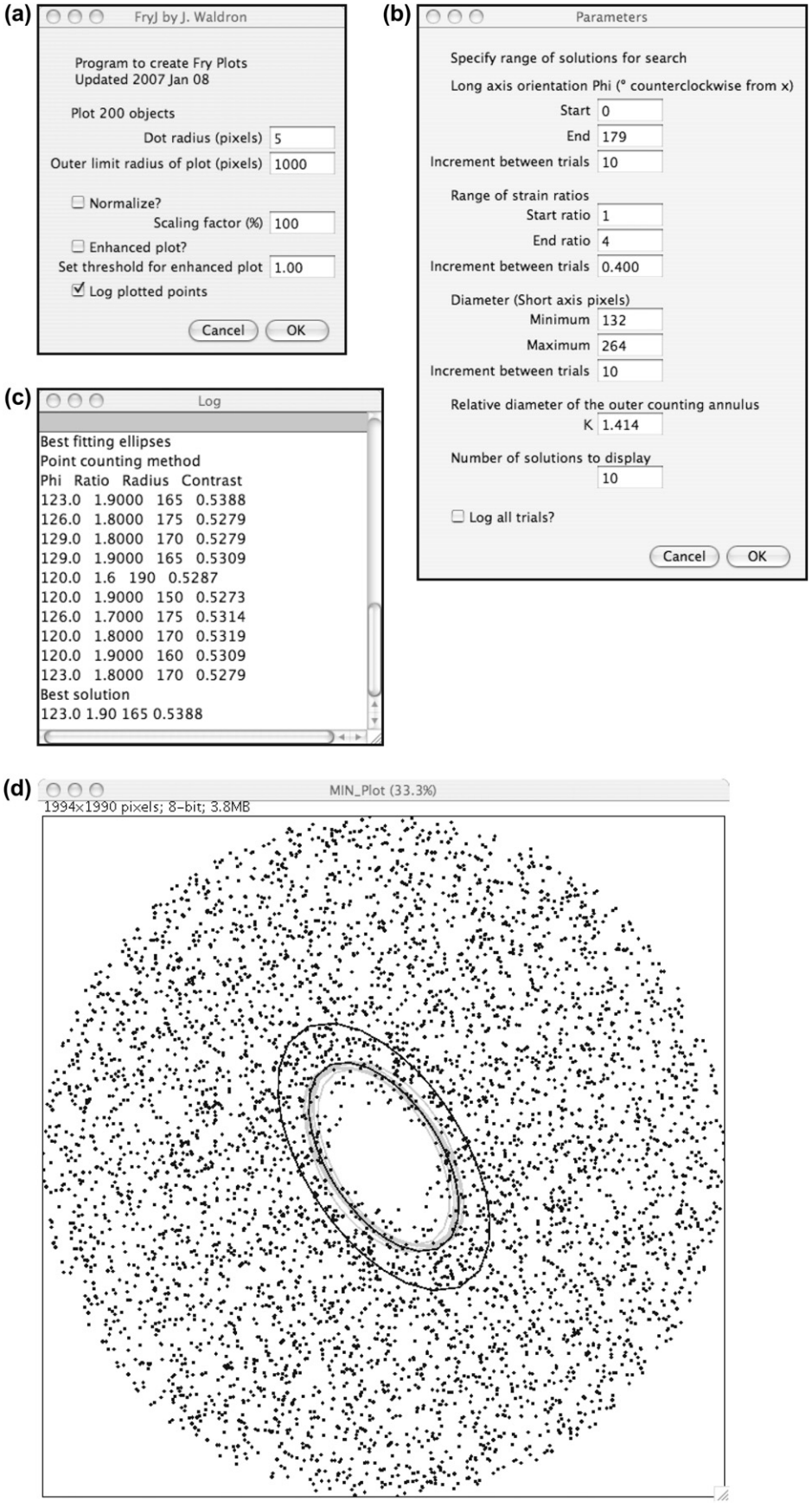


Fig. 6. Screen capture images from Fry plotting and ellipse fitting programs in image processsing software 'ImageJ'. (a) Initial dialog from macro 'FryJ', setting parameters for Fry plot. (b) Main dialog from macro 'FryJFit' setting parameters for search for optimum ellipse. (c) Numerical output from 'FryJFit' listing 10 ellipses giving highest values of fit statistic *C*. (d) Graphical output from 'FryJFit' showing ten best-fit ellipses and their parameters. Optimum ellipse is shown in black with inner and outer ellipses. Remaining best-fit ellipses are shown by inner ellipses only, in grey.

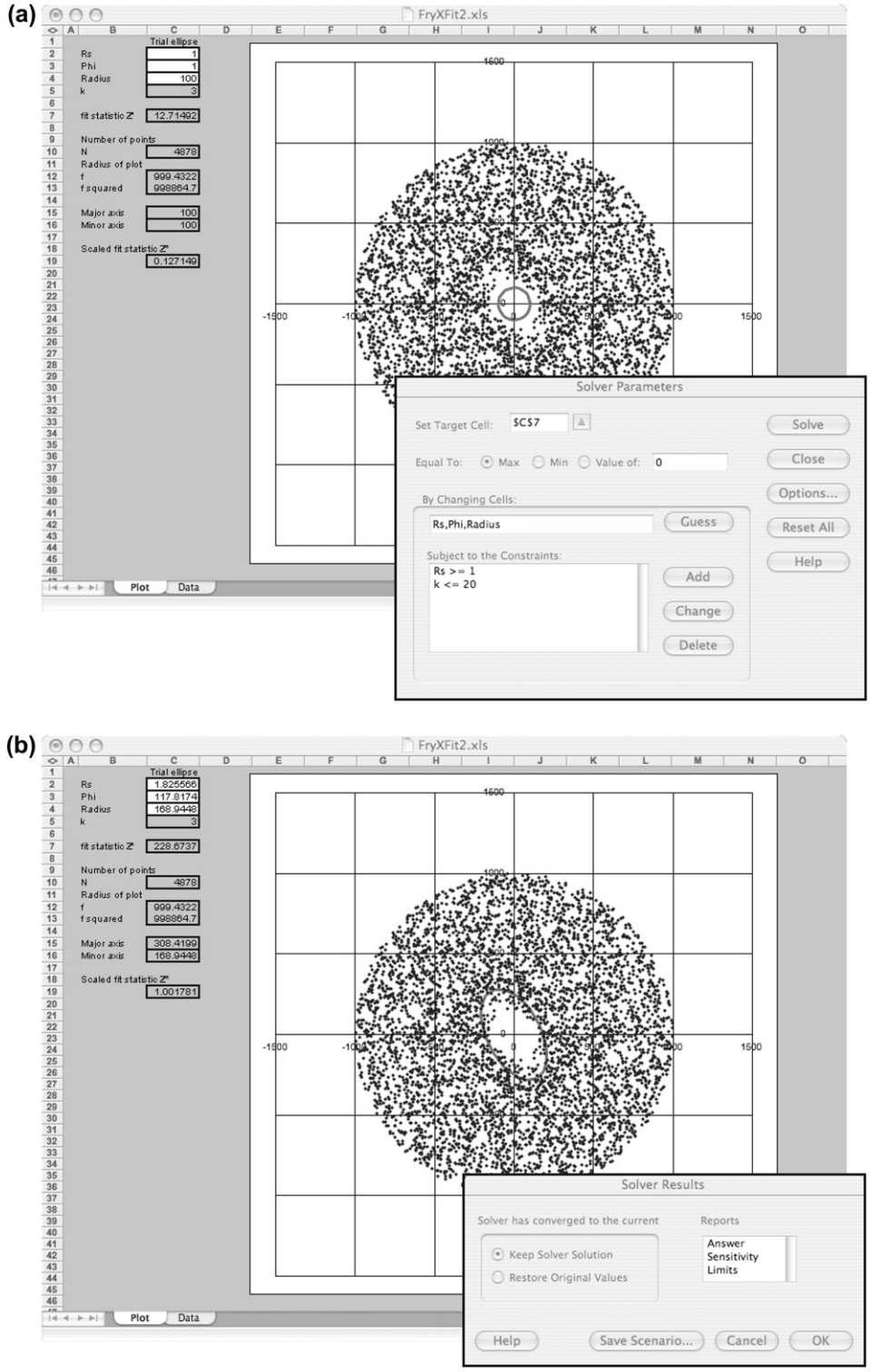


Fig. 7. Screen capture images from Excel spreadsheet FryXFit. (a) Initial conditions with Solver dialog. (b) Solution display.

different degrees of anticlustering and strain, and an artificially strained image of an undeformed sandstone. We have also applied both methods to a number of real examples of deformed rock (with unknown strain), including the dewatering pipes (Fig. 1) that provided the impetus for this study. Our testing has been aimed at determining whether the proposed methods produce estimates of strain ratio ($R$) and strain orientation ($\varphi$) that are reasonable, given the known applied strain (in the case of simulated object arrays), or the geological context (for the naturally strained rocks). We have not attempted to place confidence limits on these estimates of strain, though we suggest that future work, using a much larger number of simulated object arrays, would enable confidence limits to be determined.

### 5.1. Artificial rock images

Isotropic images containing arrays of 200 and 400 anticlustered objects were generated in ImageJ. A macro was written which randomly generates grain radii from a specified grain-size distribution and uses these values to draw circular 'grains' in an image. During a run, an initial object is placed at the centre of the blank image, and subsequent objects are positioned around it at random azimuths, with steadily increasing distance from the centre of the image. If a randomly generated position creates overlap with a previously placed object, successive alternative positions are generated until the object is successfully placed without overlap. In this way an isotropic 'snowball' of objects with specified size distribution is built up (Fig. 8a). To vary the degree of anticlustering, images having four values of sorting (standard deviation in sedimentological 'phi' units of 0.3, 0.4, 0.6 and 0.8) were used (Fig. 8a). It should be noted that the correspondence with real sediments is approximate: variable grain shape weakens the level of anticlustering in a real sample, whereas the use of normalized Fry plotting would enhance it. Also, sorting was used as a convenient proxy for anticlustering; we could equally have varied the degree of packing or used some process other than simulated 'sediment accumulation'. The results are therefore expected to be broadly applicable to anticlustered distributions of objects.

Each image was distorted using ImageJ to impose pure strains with strain ratios of 1.3, 1.8, and 2.5, with arbitrarily oriented strain axes (Fig. 8b). The resulting images were then analysed with ImageJ to list the particles, and processed with the macro FryJ to produce a Fry plot and a log of all the contained points. The macro FryJFit and the Excel

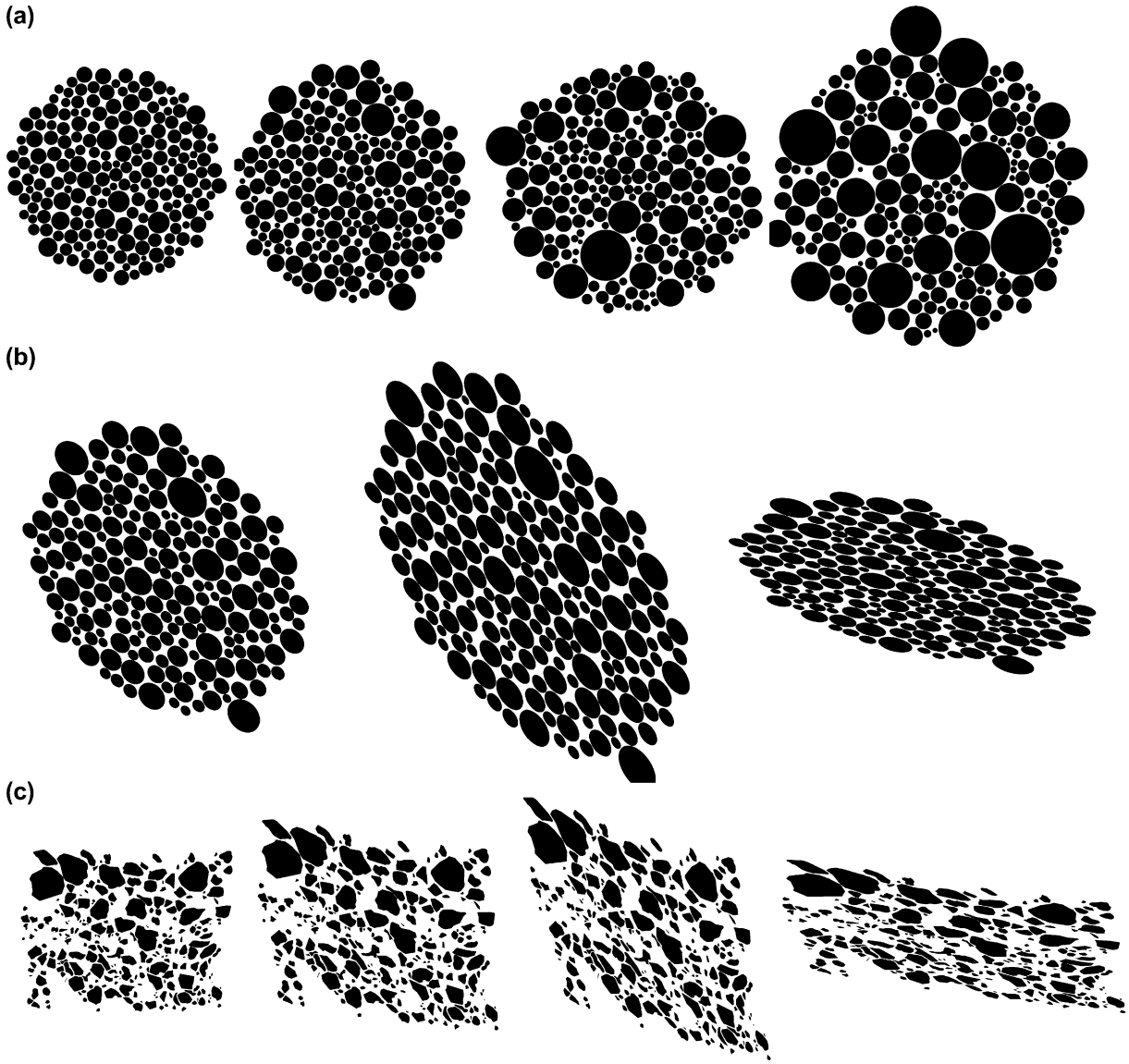


Fig. 8. Simulated arrays of particles used to generate test Fry plots. (a) Undeformed random particles with 'sorting' values of 0.3, 0.4, 0.6 and 0.8; $n = 200$ in all cases. (b) Strained images ('sorting' = 0.4) with strain ratios (A) 1.3, (B) 1.8 and (C) 2.5. (c) Image of undeformed sandstone, and three distorted images with same strains as above; $n = 245$.

spreadsheet FryXFit were used to fit ellipses to the vacancy fields.

To determine the optimum value for the parameter $k$ in the continuous function method, several samples were processed using different values of $k$. In addition, runs of the solver were carried out with 'floating' $k$, in which the solver was allowed to vary $k$, in addition to $r$, $R$, and $\varphi$, to maximize the value of $Z'$. Typical results are shown in Table 1. It was found that the 'floating' $k$ method typically yielded $k$ values between 2 and 4, and that for fixed $k$, a value of 3 produced consistently good results, in which estimated strain was close to the strain initially applied to the image. A $k$ value of 3 was used in subsequent testing.

### 5.2. Artificially strained images of a real sample

A thin section of sandstone from the Late Cretaceous to Paleocene Scollard Formation of the undeformed Cordilleran foreland basin in Alberta was photographed and traced to make an image of the framework grains (Fig. 8c). The sandstone is highly angular, and its sorting was determined by particle measurement in ImageJ to be 0.99 phi units, close to the borderline between moderately and poorly sorted. Though showing some grading in grain size (the section cuts bedding), the sample shows no perceptible grain-shape fabric. Copies of the image were strained in ImageJ, using the same strains as the simulated particle arrays.

### 5.3. Results

Results for 21 images with different values of sorting and strain are shown in Table 2. For the 'very well-sorted' artificial samples of 200 objects, both methods were able to determine the 'correct' orientation of the strain ellipse within a few degrees and the strain ratio within ±0.1. With decreasing levels of anticlustering, the precision decreased, but results were at least as good as those obtained by subjective estimation. For weakly anticlustered distributions, corresponding to the 'moderately sorted' grain sizes, strain ratios were fitted within 20% of the true value. Deviations in estimated magnitude appear greatest at the largest values of $R$. As expected, the precision in orientation varied with strain ratio; at low strain ratios the orientation of the strain ellipse was poorly constrained by the plot, whether the determination was carried out subjectively by an operator or by one of the computer methods. For the artificially deformed image of a real sandstone thin section, non-normalized Fry plots showed very indistinct vacancy fields, which would not be regarded as usable using subjective methods; the corresponding machine-determined strains were highly inaccurate, particularly in the case of the most extremely deformed. However, normalized plots from the same sample yielded much more accurate strain estimates; the most highly strained yielded the least accurate estimate of strain ratio, overestimating the correct value by 10%. In all these cases, strain axis orientation was estimated within 5°.

Table 2
Results from simulated samples and natural images with simulated strain

| | Original image | | Strain applied | | Results: continuous function method | | | Results: point-counting ellipse method | | |
|---|---|---|---|---|---|---|---|---|---|---|
| | Number of objects | Standard deviation (*phi*) | Strain ratio ($R$) | Orientation of long axis | Estimated strain ratio | Orientation of long axis | Fit measure ($Z^*$) | Estimated strain ratio | Orientation of long axis | Contrast measure ($C$) |
| Simulated rock image | | | | | | | | | | |
| 1 | 200 | 0.3 | 1.3 | 132 | 1.28 | 134.3 | 1.988 | 1.32 | 134.4 | 1.0127 |
| | 200 | | 1.8 | 123 | 1.82 | 125.2 | 1.898 | 1.84 | 122.6 | 0.9821 |
| | 200 | | 2.5 | 167 | 2.49 | 164.3 | 1.878 | 2.4 | 167.2 | 1.1154 |
| 2 | 200 | 0.4 | 1.3 | 132 | 1.25 | 126.5 | 1.403 | 1.32 | 106.8 | 0.717 |
| | 200 | | 1.8 | 123 | 1.74 | 121.6 | 1.377 | 2.04 | 116 | 0.6999 |
| | 200 | | 2.5 | 167 | 2.36 | 167.1 | 1.443 | 2.12 | 164 | 0.7875 |
| 3 | 200 | 0.6 | 1.3 | 132 | 1.29 | 110 | 1.023 | 1.54 | 124.6 | 0.5697 |
| | 200 | | 1.8 | 123 | 1.82 | 117 | 1.003 | 2.12 | 122.4 | 0.5668 |
| | 200 | | 2.5 | 167 | 2.25 | 167 | 1.066 | 2.48 | 163.6 | 0.6272 |
| 4 | 200 | 0.8 | 1.3 | 132 | 1.32 | 108.6 | 1.078 | 1.45 | 85 | 0.6135 |
| | 200 | | 1.8 | 123 | 1.85 | 113.5 | 1.058 | 1.8 | 101 | 0.6132 |
| | 200 | | 2.5 | 167 | 2.11 | 167.7 | 1.133 | 2.25 | 168 | 0.6334 |
| 5 | 400 | 0.8 | 1.3 | 132 | 1.23 | 150.5 | 0.690 | 1.36 | 109.6 | 0.4875 |
| | 400 | | 1.8 | 123 | 1.8 | 119.3 | 0.911 | 1.8 | 118 | 0.4966 |
| | 400 | | 2.5 | 167 | 2.46 | 166.5 | 0.937 | 2.25 | 167 | 0.5211 |
| Thin section | | | | | | | | | | |
| | 244 | 0.99 | 1.3 | 132 | 1.39 | 168.8 | 0.679 | 1.2 | 118.8 | 0.4851 |
| | 244 | Normalized | 1.3 | 132 | 1.36 | 136.6 | 1.821 | 1.32 | 136 | 0.9212 |
| | 244 | 0.99 | 1.8 | 123 | 1.56 | 141.6 | 0.691 | 1.63 | 115 | 0.4627 |
| | 244 | Normalized | 1.8 | 123 | 1.81 | 127.7 | 1.135 | 1.85 | 126 | 0.9481 |
| | 244 | 0.99 | 2.5 | 167 | 3.84 | 176.3 | 0.656 | 2.1 | 170 | 0.5226 |
| | 244 | Normalized | 2.5 | 167 | 2.75 | 166.4 | 1.368 | 2.95 | 167 | 1.0348 |

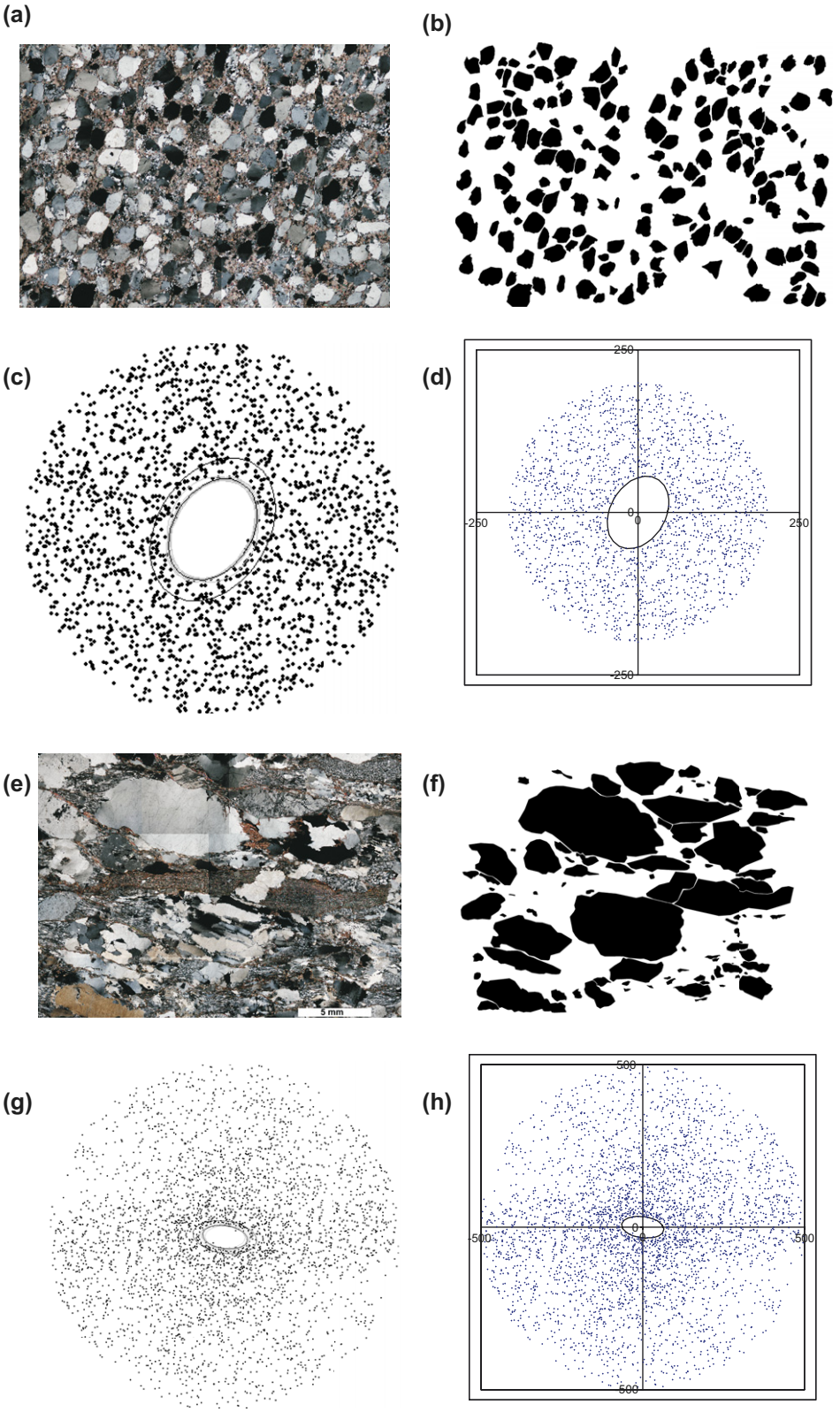


Fig. 9. Results of Fry analysis of thin sections from the Upper Kaza Group, Cariboo Mountains, British Columbia, Canada. (a) Thin section of relatively well-sorted, carbonate-cemented sandstone. (b) Grain outlines. (c) Normalized Fry plot with ellipse interpreted by FryJFit; $n = 172$. (d) Normalized Fry plot with ellipse interpreted by FryXFit. (e–h) Similar normalized plots from coarse, poorly sorted, polymictic sandstone; $n = 94$.

In general, comparing results by each method from the same sample, it was found that in most cases the continuous function method gave slightly more accurate estimates of strain ratio. The optimum values of $Z^*$ and $C$ could be used as qualitative indicators of the reliability of the results. The strongly anticlustered samples yielded $Z^*$ between 1.4 and 2 and strain ellipses within 10% of the correct strain ratio and 10° of the correct orientation. Values of $Z^*$ below 1 were associated with poorly constrained ellipses. For the point-counting method, reliable estimates of strain ratio and orientation corresponded to $C$ values greater than about 0.7.

To provide a more adequate quantification of the relationships between errors, $C$ and $Z^*$ values, a Monte Carlo approach could be adopted, by simulating a much larger number of anticlustered distributions, representing different degrees of sorting and/or packing of objects. It would then be possible to determine the relationship between the precision of strain estimates and the value or $C$ or $Z^*$. Such a determination is beyond the scope of this paper.

### 5.4. Fabric ellipse determinations from naturally deformed rocks

Both methods were applied to an investigation of sandstone turbidites of the Neoproterozoic Kaza Group (Windermere Supergroup) in the Cariboo Mountains of British Columbia, Canada. In this area, the structure is dominated by NW-trending F2 folds with cleavage that is slightly oblique to fold axial surfaces. Sedimentary structures are well preserved, and the area provides an excellent opportunity for the study of a continental-margin submarine-fan system. To interpret depositional geometries and paleocurrent distributions, tectonic strain needs to be quantified and removed. Furthermore, the slight transection of folds by cleavage suggests that deformation possibly involved a component of transpression, so that strain determinations in three-dimensional may help to quantify this component and shed light on the tectonic history. Accordingly, field observations and oriented samples of deformed sandstone were collected to quantify the strain.

#### 5.4.1. Dewatering pipes

Certain well-sorted sandstone turbidites of the Upper Kaza Group contain dewatering pipes visible on bedding-parallel sections due to differential cement with a distinctive colour, probably due to a higher iron content than the matrix (G.M. Ross, personal communication, 2003). To apply the Fry method to these structures, the pipes are assumed to be anticlustered and initially isotropically distributed due to the fact that they likely drew from roughly equal volumes of interstitial water.

To use these structures as strain markers, photographs were taken with the camera axis carefully oriented perpendicular to the bedding surface. Bedding was slightly overturned and the view in Fig. 1 is of the original under-surface. The centres of the dewatering pipes were marked as point objects and a TIFF image file was created. A standard Fry plot was generated with FryJ. The resulting Fry plot has a poorly defined vacancy field (Fig. 1b), making subjective estimates of the strain ratio difficult.

The log of the Fry plot points was analysed with FryJFit and FryXFit. Consistent results (Fig. 1c, d) were obtained from the two methods, with a strain ratio of approximately 1.7, and a long axis orientation approximately 40° clockwise from strike, roughly perpendicular to the trace of veins on bedding, but significantly oblique to the fold hinge orientation and the bedding-cleavage intersection, suggesting non-coaxial strain during folding.

#### 5.4.2. Thin sections of sandstone

Numerous oriented thin sections were cut through sandstones from the same area. Many samples showed quite variable sorting and grain shape. We prepared photomosaics of each thin section from which grain outlines were traced. Fig. 9 shows two examples, one from a relatively well-sorted sandstone with small strain in the plane of section, and one with poor sorting and larger strain. Fig. 9 (c, d, g, and h) shows the results of ellipse fitting with FryJFit and FryXFit, as applied to normalized Fry plots. In both cases, the two methods gave mutually consistent results that were also congruent with visual estimates of ellipse shape.

## 6. Conclusions

The Fry method is elegant and versatile as a means of strain determination in rocks that contain anticlustered objects, but its application has been hampered by the subjectivity of estimating the shape of the central vacancy field. Two methods proposed here provide the possibility of objectively and automatically estimating this shape. Both are based on the initial identification of objects using the public-domain, Java-based image processing program ImageJ. The point-count density method compares the density contrast between an inner elliptical field and a surrounding elliptical annulus. The maximum density contrast occurs when the dimensions of the inner ellipse coincide with those of the vacancy field. A second method that is faster, and often more accurate, uses a continuous function to measure the fit between a trial ellipse and the shape of the vacancy field. By maximizing the value of the function $Z'$, it is possible to obtain good estimates of the shape of the fabric ellipse, even with small data sets of $\sim$200 objects, provided there is a moderate degree of anticlustering. For strongly anticlustered object sets at moderate strains, estimates of the strain ratio are typically within 10% of the correct value, while the orientation of the strain axes can be located within 10°. Future work, using large numbers of random simulated samples, may be able to place confidence limits on the estimates of the strain parameters.

## Acknowledgments

We are grateful to journal reviewers Mark McNaught and Jean Crespi, and to editor Bill Dunne, for helpful and constructive reviews. This project was supported by Natural Sciences and Engineering Research Council Discovery Grant

A8508 to Waldron. Field support and facilities in the Cariboo Mountains were provided the Windermere Consortium; we are grateful to Bill Arnott and Gerry Ross for their assistance. Shar Anderson and Cory Bloomberg assisted with data collection in the field and in the laboratory, respectively. We thank Octavian Catuneanu for providing the undeformed sandstone of the Scollard Formation.

## Appendix A. Supplementary data

Supplementary data associated with this article can be found, in the online version, at doi:10.1016/j.js.2007.06.005.

## Appendix 1. Variation of point density in Fry plots for random distributions

If the parent distribution has some density (objects/area), $\rho_0$, then the expected number of objects in a circular neighbourhood with radius $f$ centred on any given object is $\pi f^2\rho_0$. If there are $n$ objects in the data set then the total number of points in the plot will be $N = n\pi f^2\rho_0$. Because the plot has area $\pi f^2$, the density of points expressed as points per unit area in the Fry plot is given by:

$$\rho = N/\pi f^2 = n\rho_0 \tag{10}$$

In fitting curves to Fry plots, however, we are interested in the density of points with respect to radius. The number of points per unit radius is here represented by $\rho'$.

Consider a random distribution Fry plot of radius $f$, containing $N$ points. The area of a thin annulus (Fig. 2) of width d$r$ located at radius $r$ is approximated by:

$$A = 2\pi r\,\mathrm{d}r \tag{11}$$

and the number of points contained therein is:

$$\mathrm{d}N = A\rho = 2Nr\,\mathrm{d}r/f^2 \tag{12}$$

Then the radial density $\rho'$ is found by:

$$\rho\prime = \mathrm{d}N/\mathrm{d}r = 2Nr/f^2 = 2\pi\rho r \tag{13}$$

## Appendix 2. Point-density contrast

The densities of points in the annulus and the inner ellipse (Fig. 4) are:

$$\rho_{\mathrm{out}} = \frac{N_{\mathrm{out}}}{\left(K^2-1\right)\pi r_1 r_2} \quad \rho_{\mathrm{in}} = \frac{N_{\mathrm{in}}}{\pi r_1 r_2} \tag{14}$$

where $N_{\mathrm{out}}$ and $N_{\mathrm{in}}$ are the numbers of points in the annulus and inner ellipse, respectively; $r_1$ and $r_2$ are the major and minor radii of the inner ellipse; and $K$ is the ratio of the radii of the outer ellipse to those of the inner ellipse.

Then the density contrast ($C$) is given by:

$$C = \frac{\rho_{\mathrm{out}}-\rho_{\mathrm{in}}}{\rho} = \frac{\left(N_{\mathrm{out}}/\left(K^2-1\right)\pi r_1 r_2\right) - \left(N_{\mathrm{in}}/\pi r_1 r_2\right)}{N/\pi f^2} = \frac{f^2}{N r_1 r_2}\left(\frac{N_{\mathrm{out}}}{\left(K^2-1\right)} - N_{\mathrm{in}}\right) \tag{15}$$

## Appendix 3. Normalizing $Z$ for variations in plot size and $k$

To compare values of $Z$, a summed measure of density contrast (Eq. (7)), calculated for different values of the constant $k$, we need to correct for the fact that the maximum possible value of the single point contribution $z$ is lowered, and also that the value of $Z$ effectively samples a smaller part of the Fry plot, as $k$ increases. In addition, to compare values of $Z$ for different sample sizes, we need to correct for sample size and plot radius.

The number of points expected within a small increment of radius d$r$ is given (Appendix 1) by:

$$\mathrm{d}N = \rho'\,\mathrm{d}r = 2\pi\rho r\,\mathrm{d}r \tag{16}$$

and the component of $Z$ corresponding to this interval is obtained by multiplying this number of points by $z$ (Eq. (6))

$$\mathrm{d}Z = z\,\mathrm{d}N = \frac{x}{r}\mathrm{e}^{-(kx)^2}2\pi\rho r\,\mathrm{d}r = 2\pi\rho x\mathrm{e}^{-(kx)^2}\mathrm{d}r \tag{17}$$

Therefore the probability density of $z$ is given by:

$$p(x) = \frac{\mathrm{d}Z}{\mathrm{d}r} = 2\pi\rho x\mathrm{e}^{-(kx)^2} \tag{18}$$

Fig. 5 shows a graph of probability plotted against $x$. The value of $Z$ will vary as the integral of this function. To explore the effect of variations in $k$ on this integral we determine the area under the positive part of the curve:

$$\int_{x=0}^{\infty} p(x)\,\mathrm{d}x = \int_{0}^{\infty} 2\pi\rho x\mathrm{e}^{-(kx)^2}\mathrm{d}x = 2\pi\rho/2k^2 = \pi\rho/k^2 \tag{19}$$

Hence for comparison between plots with the same grain size but different numbers of points and radii, and to compare the effects of different $k$ values, we calculate a normalized value of $Z$:

$$Z' = \frac{k^2 f^2}{N}\sum_{i=1}^{N} z_i \tag{20}$$

## Appendix 4. Effect of object spacing

The optimum value of $Z'$ as defined in Appendix 3 was found to scale linearly with object size in experiments using point populations that differed only in spacing, but were otherwise identical. Two effects come into play here. First, the values of $z$ for individual points are reduced by a factor $1/r$ with increasing

distance from the centre of the Fry plot. Hence $Z'$ is reduced proportionally to the radius of the optimal ellipse.

Secondly, the effective number of points sampled by $Z'$ is increased proportional to the area of the optimal ellipse. This is given by $E = \pi r_1 r_2$ where $r_1$ is the major axis of the ellipse and $r_2$ is the minor axis.

To compare populations of points having different vacancy field sizes, it is necessary to correct for these factors. The net effect of these two factors is that $Z'$ is scaled linearly in proportion to the mean radius of the optimal ellipse, given by $\sqrt{(r_1 r_2)}$. Accordingly, to compare Fry plots derived from populations of objects with different anticluster diameters (for granular materials, different grain size), we define a scaled value of the optimal $Z'$ represented by $Z^*$:

$$Z^* = \frac{Z'_{\text{opt}}}{\sqrt{r_1 r_2}} \tag{21}$$

## References


Abramoff, M.D., Magelhaes, P.J., Ram, S.J., 2004. Image processing with ImageJ. Biophotonics International 11, 36–42.

Ailleres, L., Champenois, M., 1994. Refinements to the Fry method (1979) using image processing. Journal of Structural Geology 16, 1327–1330.

Crespi, J.M., 1986. Some guidelines for the practical application of Fry's method of strain analysis. Journal of Structural Geology 8, 799–808.

Dunne, W.M., Onasch, C.M., Williams, R.T., 1990. The problem of strain-marker centers and the Fry method. Journal of Structural Geology 12, 933–938.

Erslev, E.A., 1988. Normalized center-to-center strain analysis of packed aggregates. Journal of Structural Geology 10, 201–209.

Erslev, E.A., Ge, H., 1990. Least-squares center-to-center and mean object ellipse fabric analysis. Journal of Structural Geology 12, 1047–1059.

Fry, N., 1979. Random point distributions and strain measurement in rocks. Tectonophysics 60, 89–105.

Hanna, S.S., Fry, N., 1979. A comparison of methods of strain determination in rocks from southwest Dyfed (Pembrokeshire) and adjacent areas. Journal of Structural Geology 1, 155–162.

Longiaru, S., Bhattaharyya, T., 1985. Computer based experimental studies of the Fry method of strain analysis on 2- and 3-dimensional grain populations. Abstracts with Programs – Geological Society of America 17, 646.

McNaught, M., 1994. Modifying the normalized Fry method for aggregates of non-elliptical grains. Journal of Structural Geology 16, 493–503.

Onasch, C.M., 1986. Ability of the Fry method to characterize pressure-solution deformation. Tectonophysics 122, 187–193.

Ramsay, J.G., 1967. Folding and Fracturing of Rocks. McGraw Hill, San Francisco.

Ramsay, J.G., Huber, M.I., 1983. The Techniques of Modern Structural Geology. Volume 1: Strain Analysis. Academic Press, London.

Waldron, J.W.F., Jensen, L.R., 1985. Sedimentology of the Goldenville Formation, Eastern Shore, Nova Scotia. Geological Survey of Canada Paper 85-15.

Waldron, J.W.F., 1988. Determination of finite strain in bedding surfaces using sedimentary structures and trace fossils: a comparison of techniques. Journal of Structural Geology 10, 273–281.